The Astrophysical Journal Letters, 718:L181–L184, 2010 August 1 doi:10.1088/2041-8205/718/2/L181

A BIPOLAR OUTFLOW FROM THE MASSIVE PROTOSTELLAR CORE W51e2-E

Hui Shi[1], Jun-Hui Zhao[2], and J. L. Han[1]
[1] National Astronomical Observatories, Chinese Academy of Sciences, 20A DaTun Road, Beijing 100012, China; shihui@nao.cas.cn, hil@nao.cas.cn
[2] Harvard-Smithsonian Center for Astrophysics, 60 Garden Street, Cambridge, MA 02138, USA; jzhao@cfa.harvard.edu
Received 2010 April 20; accepted 2010 June 17; published 2010 July 15

ABSTRACT

We present high-resolution images of the bipolar outflow from W51e2, which are produced from the Submillimeter Array archival data observed for CO(3–2) and HCN(4–3) lines with angular resolutions of $0\farcs8 \times 0\farcs6$ and $0\farcs3 \times 0\farcs2$, respectively. The images show that the powerful outflow originates from the protostellar core W51e2-E rather than from the ultracompact H II region W51e2-W. The kinematic timescale of the outflow from W51e2-E is about 1000 yr, younger than the age (∼5000 yr) of the ultracompact H II region W51e2-W. A large mass-loss rate of $\sim 1 \times 10^{-3}\ M_\odot\ \mathrm{yr}^{-1}$ and a high mechanical power of 120 $L_\odot$ are inferred, suggesting that an O star or a cluster of B stars are forming in W51e2-E. The observed outflow activity along with the inferred large accretion rate indicates that at present W51e2-E is in a rapid phase of star formation.

Key words: ISM: individual objects (W51e2) – ISM: jets and outflows – stars: formation

Online-only material: color figures

1. INTRODUCTION

Molecular outflows from protostellar cores provide a critical means to transport angular momentum from the accretion disk into the surrounding environment. The molecular outflows and infalls vigorously affect the turbulence and dissipation of molecular gas in molecular cores, playing an important role in the formation and evolution of massive stars. Observations of outflows can reveal the history of mass-loss processes in a protostellar system. In particular, high angular resolution observations of outflows can precisely determine the origin of an outflow and separate the outflow from the infall in a protostellar core. Nearly half of the observed molecular outflows are driven by massive protostars ($L_{\rm bol} > 10^3\ L_\odot$) and have a typical dynamical age of $\sim 10^4$ yr and a mass outflow rate of $\sim 10^{-3}\ M_\odot\ \mathrm{yr}^{-1}$ (e.g., Churchwell 2002).

W51e2, located at a distance of 5.1 kpc (Xu et al. 2009), is a prototypical core for massive star formation. The molecular core is associated with an ultracompact H II region (e.g., Scott 1978; Gaume et al. 1993) and a possible inflow (e.g., Ho & Young 1996; Zhang et al. 1998; Sollins et al. 2004; Shi et al. 2010). With high-resolution observations, using the Submillimeter Array (SMA)[3] at the wavelengths of 0.85 and 1.3 mm, W51e2 was resolved into four sub-cores (Shi et al. 2010) including the ultracompact H II region (W51e2-W) and a massive protostellar core (W51e2-E). From the analysis of the HCN(4–3) absorption line, Shi et al. (2010) showed that the bright dust core, W51e2-E, $0\farcs9$ east of W51e2-W, dominates the mass accretion in the region. A bipolar outflow has been detected in the W51e2 region (Keto & Klaassen 2008) based on the SMA observations of CO(2–1) line with an angular resolution of $\sim 1''$. However, the resolution of the CO(2–1) observation was not adequate to determine the origin of the molecular outflow.

High angular resolution observations are imperative to identify the origin of the molecular outflow. In this Letter, we present high-resolution images of the bipolar outflow using the SMA data of the HCN(4–3) and CO(3–2) lines observed at 0.85 and 0.87 mm with angular resolutions of $0\farcs3 \times 0\farcs2$ and $0\farcs8 \times 0\farcs6$, respectively. We determine and discuss the physical properties of W51e2-E and W51e2-W cores, and assess the roles of the outflow in the process of massive star formation in W51e2.

2. DATA REDUCTION

The interferometer data for the HCN(4–3) and CO(3–2) lines at $\nu_0 = 354.505$ and 345.796 GHz were acquired from the SMA archive, observed on 2007 June 18 and 2008 July 13 with the "very extended" and "extended" array configurations, respectively. The reduction for the HCN(4–3) line data was made in Miriad (Sault et al. 1995) following the reduction instructions for SMA data,[4] which has been discussed in Shi et al. (2010). We constructed image cubes for the HCN(4–3) line with a channel width of 1 km s^{-1} and an FWHM beam of $0\farcs33 \times 0\farcs24$ (P.A. = 68°). The typical rms noise in a channel image is 0.07 Jy beam^{-1}.

The CO(3–2) line is included in the SMA observations at 0.87 mm for the polarization study of W51e2 that was discussed by Tang et al. (2009). The cross-polarization data were flagged before processing the data in Miriad. The data scans on 3C454.3 were used for bandpass calibration. QSO J1751 + 096 was used for calibration of the complex gains, and Uranus was used to determine the flux-density scale. The continuum level was subtracted from the line channels using UVLIN. The continuum-free line data were used for imaging with the natural weighting and a channel width of 1 km s^{-1}. A typical rms noise of 0.14 Jy beam^{-1} and an FWHM beam of $0\farcs79 \times 0\farcs62$ (P.A. = −80°) were achieved for a channel image.

The shortest UV lengths in the visibility data are 30 kλ and 54 kλ, corresponding to angular sizes of about $7''$ and $4''$ for the CO and HCN structure, respectively. The compact structure (<3″) of the outflow in both CO and HCN appears to be adequately sampled in the SMA observations. However, the total line flux density of the outflow may be underestimated due to the missing short spacing. From a visibility model for

[3] The Submillimeter Array is a joint project between the Smithsonian Astrophysical Observatory and the Academia Sinica Institute of Astronomy and Astrophysics and is funded by the Smithsonian Institution and the Academia Sinica.

[4] http://www.cfa.harvard.edu/sma/miriad

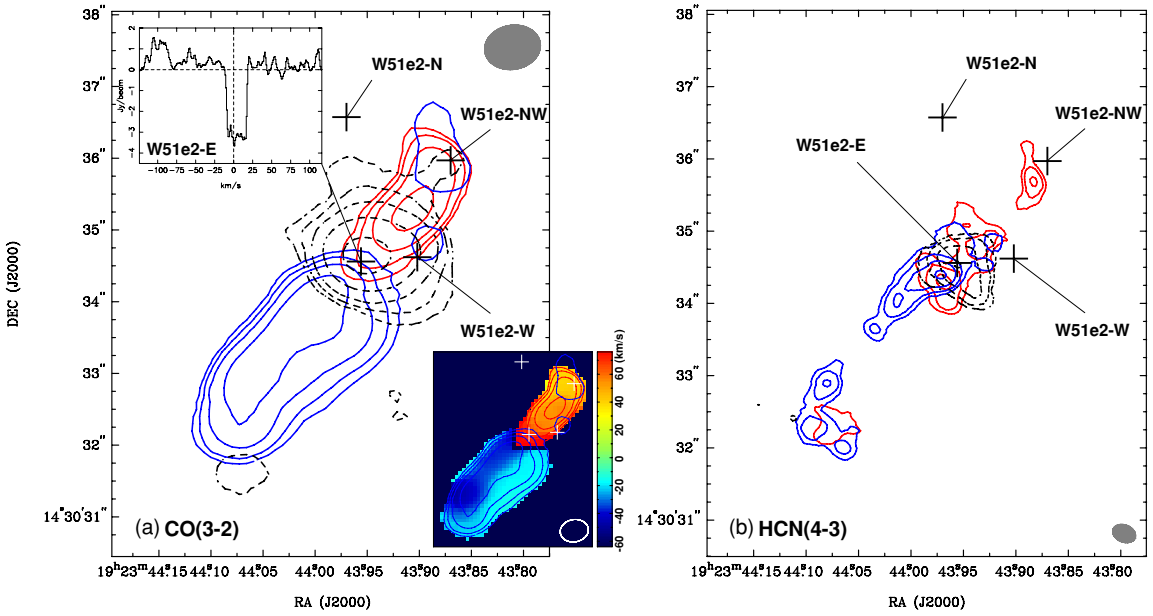

Figure 1. (a) SMA image of W51e2 for CO(3–2) line emission at 0.87 mm, integrated from the velocity ranges of −124 to −12 km s^{-1} (blue contours) and +10 to +116 km s^{-1} (red contours). The integrated absorption (dashed contours) corresponds to the velocity range −11 to +9 km s^{-1}. The contours are $\pm 5\sigma \times 2^n$ Jy beam^{-1} km s^{-1} ($n = 0, 1, 2, 3, \ldots$), where σ = 1.2, 1.3, and 0.63 Jy beam^{-1} km s^{-1} for the blueshifted, redshifted emission, and absorption, respectively. The FWHM beam is 0.″79 × 0.″62 (P.A. = −80°) shown at top right. The top left inset is the CO(3–2) absorption spectrum toward W51e2-E. The bottom right inset is the intensity-weighted velocity image derived from the CO(3–2) line data (the color wedge representing the velocity range −64 to +76 km s^{-1} relative to $V_{\rm LSR}$ = 53.9 km s^{-1}), excluding the absorption and insignificant emission (<3σ). Crosses mark the positions of the sub-cores in W51e2 (Shi et al. 2010). (b) SMA image of W51e2 for HCN(4–3) line at 0.85 mm, integrated from the same velocity range as CO(3–2) in (a). The contours are $\pm 5\sigma \times 2^n$ Jy beam^{-1} km s^{-1} ($n = 0, 1, 2, 3, \ldots$), where σ = 0.71, 0.67, and 0.31 Jy beam^{-1} km s^{-1} for the blueshifted, redshifted emission, and absorption, respectively. The FWHM beam is 0.″33 × 0.″24 (P.A. = 68°) shown at bottom right.

(A color version of this figure is available in the online journal.)

the outflow source with a *uv* coverage identical to the SMA data, we assess that ⩽2% and ⩽8% in the CO and HCN line flux densities may be underestimated, respectively.

3. RESULTS

3.1. Morphologies of the Bipolar Outflow

Figure 1(a) shows the CO(3–2) image of W51e2 for the integrated blueshifted (−124 to −12 km s^{-1}) and redshifted (+10 to +116 km s^{-1}) emission and absorption (−11 to +9 km s^{-1}) with respect to the systemic velocity of $V_{\rm LSR}$ = 53.9 km s^{-1} (Shi et al. 2010). The outflow velocities discussed throughout the Letter are with respect to this systemic velocity. The low velocity limits were determined by the velocities at the boundary of the absorption region. The high velocity limits correspond to the velocities at which the high-velocity wing profiles drop to the 1σ level. The ranges of velocities for the outflow wings are also valid for the CO(2–1) and HCN(4–3) line profiles. The CO(3–2) line profiles appear to be contaminated by three narrow ($\Delta V_{\rm FWHM} \approx 6$ km s^{-1}) anonymous lines at the velocities of –104, –89, and +70 km s^{-1}. Prior to integrating the CO(3–2) line from the outflow, the line emission in the velocity ranges from –117 to –79 and from +62 to +76 km s^{-1} is blanked. Thus, about 20% and 10% of the line fluxes are missing in the blueshifted and redshifted outflow lobes shown in Figure 1(a), respectively.

The CO(3–2) image shows a stronger blueshifted lobe in the southeast with a position angle of 140° ± 6° (from north to east) and a weaker redshifted lobe in northwest (−40° ± 11°), which are in agreement with the outflow structure revealed in the CO(2–1) image (Keto & Klaassen 2008). With Gaussian fitting, we determined the intrinsic sizes of 2.″3 × 0.″6 and 1.″1 × 0.″6 for the blueshifted and redshifted lobes, respectively. Our high-resolution CO(3–2) image clearly shows that the molecular bipolar outflow originates from W51e2-E (the protostellar core) rather than W51e2-W (the ultracompact H II region). The bright emission ridge along the northeast edge of the blueshifted lobe corresponds to a high-velocity component of the outflow, or an outflow jet (see the velocity distribution image in the lower right inset of Figure 1(a)). The weak, relatively extended emission along the southwest edge of the blueshifted lobe may indicate a backflow of the molecular gas from the interaction between the outflows and the medium surrounding the W51e2 core. In addition, a velocity gradient is present along the major axis of the redshifted lobe, with higher velocities near the core, indicating that the gas in the redshifted outflow is decelerated. By averaging the intensity-weighted velocities along the bright emission ridges in both the blueshifted and redshifted lobes, we infer the mean radial velocities of $\bar{V}_{\rm blue} = -34 \pm 7$ and $\bar{V}_{\rm red} = +52 \pm 2$ km s^{-1} for the outflow lobes. The CO(3–2) spectrum toward W51e2-E also shows a large fraction of absorption to be redshifted relative to the systemic velocity (top left inset of Figure 1(a)), suggesting the presence of infalling gas, which agrees with the results from the observations of the CO(2–1) and HCN(4–3) lines (Shi et al. 2010).

The HCN(4–3) image in Figure 1(b) shows the high-density gas components in the bipolar outflow. At the resolution of 0.″3 × 0.″2, the SMA image unambiguously verifies that W51e2-E is the driving source for the bipolar outflow in the region. We also noticed that the HCN emission traces the northeast edge of the blueshifted lobe where the CO(3–2) emission shows a sharp gradient both in intensity and velocity, suggesting that the line emission of the molecular HCN is likely enhanced near

Table 1
Outflow Parameters from CO(3–2) and CO(2–1) Lines

Quantities	CO(3–2)		CO(2–1)	
	Blue	Red	Blue	Red
V range (km s^{-1})	−124 to −12	+10 to +116	−124 to −12	+10 to +116
$\bar{V}$ (km s^{-1})	-34 ± 7	$+52 \pm 2$	...	...
ΔV (km s^{-1})[a]	19 ± 5	33 ± 8	14 ± 2	19 ± 4
Outflow intrinsic size $\theta_{\rm Maj}$ ($''$)	2.3 ± 0.3	1.1 ± 0.4	...	...
Outflow intrinsic size $\theta_{\rm Min}$ ($''$)	0.6 ± 0.5	0.6 ± 0.6	...	...
Outflow P.A. ($^\circ$)	140 ± 6	-40 ± 11	...	...
$\int \Delta I(v)dv$ (Jy beam^{-1} km s^{-1})[a]	120^{+30}_{-18}	80^{+15}_{-12}	59 ± 6	25 ± 3
$\Delta I(\nu_{\rm p})$ (Jy beam^{-1})[a]	6.5 ± 1.0	2.4 ± 0.4	4.3 ± 0.4	1.3 ± 0.2
$\Delta T_{\rm L}(\nu_{\rm p})$ (K)[a,b]	112 ± 17	41 ± 7	>100	>30
$f_{\rm B}$[b]	0.6	0.6	$\leqslant 1$	$\leqslant 1$
$T_{\rm ex}$ (K)	120	65	120	65
$\tau_{\rm L}(\nu_{\rm p})$	3.9	1.3	1.9	0.7
$N_{\rm H_2}$ (10^{22} cm^{-2})[c]	6.4	1.3	...	...
$M_{\rm out}$ ($M_\odot$)	1.3	0.1	...	...
$t_{\rm out}$ (yr)[d]	1600/tan(i)	500/tan(i)	...	...

Notes.
[a] The quantities at the maximum positions of the CO(3–2) flux. $\Delta V = \int \Delta I(v)dv / \Delta I(\nu_{\rm p})$.
[b] The beam filling factor ($f_{\rm B}$) is the ratio of the minor-axis size to the beam size projected on the minor axis and $\Delta T_{\rm L}(\nu_{\rm p}) = \frac{c^2}{2k}\nu_{\rm p}^{-2}\Delta I(\nu_{\rm p}) f_{\rm B}^{-1}$.
[c] $N_{\rm H_2} = 8 \times 10^{17} T_{\rm ex} \exp\left(\frac{16.6}{T_{\rm ex}}\right)\left[1 - \exp(\frac{-16.6}{T_{\rm ex}})\right]^{-1} \int \tau_L dv \approx 5 \times 10^{16}\,{\rm cm^{-2}} T_{\rm ex}^2 \exp\left(\frac{16.6}{T_{\rm ex}}\right)\tau_L(\nu_{\rm p})\Delta V$ for CO(3–2) assuming an abundance of $[N_{\rm CO}]/[N_{\rm H_2}] = 10^{-4}$.
[d] i is the angle between the major axis of outflow and line of sight.

the shocked or compressed regions of an outflow (Bachiller & Perez Gutierrez 1997). In addition, at the southeastern tip of the blueshifted outflow lobe, an "L" shape structure is detected in the HCN(4–3) emission with a double spectral feature at $V \approx -14$ and +16 km s^{-1}, each of the spectral profiles having a line width of $\Delta V_{\rm FWHM} \sim 15$ km s^{-1}. The HCN line emission suggests that the gas in the region is swept up by the suspected bow shock at the tip of the outflow.

The polarization emission detected in the W51e2 region shows a "hourglass" shape in magnetic fields, which is probably related to the gas infall and disk rotation (Tang et al. 2009). Our images for the bipolar outflow in both the CO(3–2) and HCN(4–3) lines (Figures 1(a) and (b)) show that, located near the "hourglass" center, W51e2-E appears to be the energy source responsible for both the magnetic fields and the bipolar outflow. The "hourglass" structure appears to slightly extend along the major axis of the outflow, suggesting that the magnetic fields might also be tangled with the outflow motions.

3.2. Physical Properties

The bipolar outflows from W51e2-E have been detected in both CO(3–2) and CO(2–1) with the SMA. In order to assess the physical conditions of the outflow gas, we re-processed the CO(2–1) data and convolved the CO(3–2) image to the same beam size as that of the CO(2–1) image ($1\farcs4 \times 0\farcs7$). For both the CO(3–2) and CO(2–1) lines, the line peak ($v = \nu_{\rm p}$) brightness temperatures $\Delta T_L(\nu_{\rm p})$ of the blueshifted and redshifted line profiles can be determined from the maximum positions of the CO(3–2) line fluxes in Figure 1. Then, the optical depth at the line peak can be estimated if the gas is in local thermal equilibrium (LTE; Rohlfs & Wilson 2004) and the cosmic microwave background (CMB) radiation is negligible:

$$\tau_L(\nu) = -\ln\left[1 - \frac{\Delta T_L(\nu)}{T_0(\nu)}(e^{\frac{T_0(\nu)}{T_{\rm ex}}} - 1)\right], \quad (1)$$

where $T_{\rm ex}$ is the excitation temperature of the transition and $T_0(\nu) = h\nu/k$. Thus, each of $\tau(\nu)_{(3-2)}$ and $\tau(\nu)_{(2-1)}$ can be independently determined from Equation (1) at a given $T_{\rm ex}$. On the other hand, under the assumption of LTE, the optical-depth ratio between CO(3–2) and CO(2–1) can be independently expressed as

$$\frac{\tau_L(\nu)_{(3-2)}}{\tau_L(\nu)_{(2-1)}} = \frac{(S\mu^2)_{(3-2)}}{(S\mu^2)_{(2-1)}} \frac{e^{\frac{T_0(3-2)}{T_{\rm ex}}} - 1}{e^{\frac{T_0(2-1)}{T_{\rm ex}}} - 1} e^{-\frac{T_0(3-2)}{T_{\rm ex}}}, \quad (2)$$

where S and μ are the line strength and the permanent electric dipole moment, respectively. For the two given transitions, such as CO(3–2) and CO(2–1), the ratio of the optical depth ($\tau_{L(3-2)}/\tau_{L(2-1)}$) depends only on the excitation temperature $T_{\rm ex}$ (Equation (2)). By giving an initial value of $T_{\rm ex}$, the three unknown quantities ($\tau_{L(3-2)}$, $\tau_{L(2-1)}$, and $T_{\rm ex}$) can be solved with a few iterative steps from Equations (1) and (2), constrained by the measured quantities $\Delta T_{L(3-2)}$ and $\Delta T_{L(2-1)}$ for each of the blueshifted and redshifted lobes.

Table 1 summarizes the results of the physical parameters determined for the molecular outflow. For the quantities directly determined from the CO images, the estimated 1σ uncertainties are given. The excitation temperatures of 120 and 65 K are derived for the blueshifted and redshifted CO outflow lobes, respectively. The optical depths of the blueshifted CO lines are $\tau_{L(3-2)} = 3.9$ and $\tau_{L(2-1)} = 1.9$, and the redshifted lobe are $\tau_{L(3-2)} = 1.3$ and $\tau_{L(2-1)} = 0.7$. Uncertainties of ~30% in the derived values for $T_{\rm ex}$ and τ_L are mainly due to the uncertainties in the determination of the line flux densities. The H_2 column density (6.4×10^{22} cm^{-2}) in the blueshifted lobe appears to be a few times greater than the value derived from the redshifted lobe (1.3×10^{22} cm^{-2}). Considering the intrinsic size of the outflow, we infer that the total outflow mass is about 1.4 $M_\odot$. From the intrinsic sizes ($\theta_{\rm Maj}$) and the intensity-weighted mean velocity ($\bar{V}$) of the outflow components, the kinematic timescale ($t_{\rm out}$) is

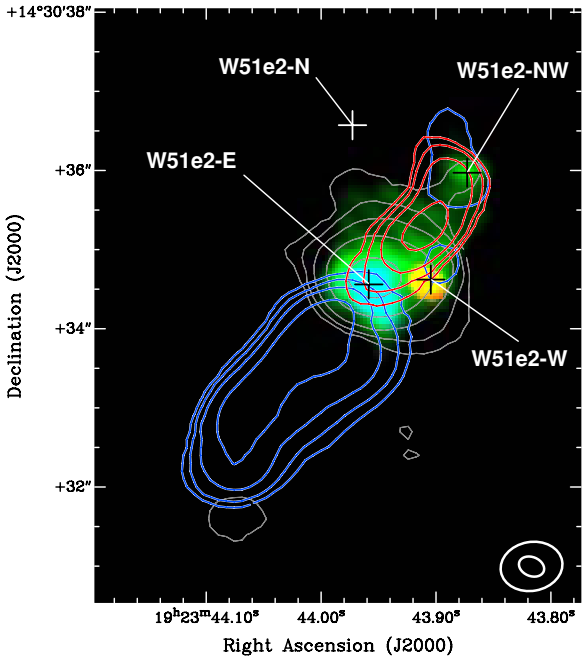

Figure 2. RGB composition image of H26α emission (red), 0.85 mm continuum emission (green), and HCN(4–3) absorption (blue) observed with the SMA at a resolution of $0\farcs33 \times 0\farcs24$ (P.A. $= 68°$; Shi et al. 2010) overlaid with the contour map of CO(3–2) outflow (red and blue) and absorption (gray; Figure 1(a)). Crosses mark the positions of the sub-cores.

(A color version of this figure is available in the online journal.)

found to be ~1000 yr if the outflow inclination angle is taken as $i \sim 45°$. Therefore, the mass-loss rate and momentum rate are $1 \times 10^{-3}\,M_\odot$ yr^{-1} and $0.04\,M_\odot$ km s^{-1} yr^{-1} from W51e2-E, respectively. The mass-loss rate has the same order of magnitude as the value of the accretion rate ($>1 \times 10^{-3}\,M_\odot$ yr^{-1}; Shi et al. 2010) derived from the HCN(4–3) absorption line toward W51e2-E. The momentum rate corresponds to a mechanical power of $120\,L_\odot$, which is at least an order of magnitude greater than that of an early type B star (e.g., Churchwell 1999; Arce et al. 2007), suggesting that the protostellar core W51e2-E is forming an O type star or a cluster of B type stars.

4. DISCUSSIONS

The current star formation activities in the W51e2 complex are shown by the powerful bipolar outflow originating from W51e2-E, in contrast to the ultracompact H II region W51e2-W detected at 6 cm (Scott 1978). The central region of W51e2-W ($<0\farcs06$), characterized by a hypercompact H II component (see the H26α line emission region in Figure 2) with $T_e = 12{,}000$ K, is surrounded by an expanding ionized component with a mean temperature of 4900 K (Shi et al. 2010). The mean density of 3.0×10^5 cm^{-3} and a Lyman photon rate of 3.0×10^{48} s^{-1} were also derived. Using a classic model for the expansion of an H II region (Garay & Lizano 1999), we estimated the dynamic age of the H II region as the time of the sound wave traveling from the initial ionization front at a radius close to the Strömgren radius (r_s; Strömgren 1939) to the current ionization front at a radius of r_i:

$$t = \frac{4}{7}\left[\left(\frac{r_i}{r_s}\right)^{7/4} - 1\right]\frac{r_s}{C_{\rm II}}. \quad (3)$$

Here r_i can be determined from radio continuum observations of the H II region, we adopted the size of $<2\farcs5$ which corresponds to $r_i < 0.03$ pc from the result of 3.6 cm continuum observation by Mehringer (1994). We derived the Strömgren radius of 0.008 pc using the mean physical parameters inferred above. The sound speed of the ionized medium is $C_{\rm II} = \sqrt{\gamma k T_e/m_p}$, where m_p is the mass of the proton and k is the Boltzmann constant. Assuming the adiabatic index $\gamma = \frac{5}{3}$ and an average $T_e = 4900$ K, we found $C_{\rm II} \approx 8.2$ km s^{-1}. Therefore, the dynamic age for the ultracompact H II region W51e2-W is about 5000 yr, which appears to be a few times older than the outflow from W51e2-E (see $t_{\rm out}$ in Table 1).

High-resolution observations of absorption spectra of the HCN(4–3) from W51e2-E and W51e2-W show that at present W51e2-E dominates the gas accretion from the molecular core W51e2 (see the HCN(4–3) absorption region, blue color in Figure 2). If the accretion rate is a constant of $1.3 \times 10^{-3}\,M_\odot$ yr^{-3} (Shi et al. 2010), W51e2-E would have accreted a total of $\sim 6\,M_\odot$ over the 5000 yr period, <5% of the total mass ($140\,M_\odot$; Shi et al. 2010) of the sub-core. Thus, most of the mass accumulation for W51e2-E probably occurred before the star(s) formed in the ultracompact H II region W51e2-W. After an O8 star or a cluster of B type stars formed in W51e2-W, the overwhelming radiation pressure and strong turbulence in W51e2-W halted the accretion in the sub-core region. Therefore, W51e2-E might speed up its formation of stars since W51e2-W is no longer competing for accretion.

In summary, a bipolar molecular outflow in W51e2 is confirmed and the massive protostellar core W51e2-E is identified to be the origin of this powerful outflow. In comparison to the ultracompact H II region W51e2-W, W51e2-E appears to be the dominant accretion source at present, where the active formation of massive stars takes place.

We thank Prof. Ed Churchwell and the referee for helpful comments. H.S. and J.L.H. are supported by the National Natural Science Foundation (NNSF) of China (10773016, 10821061, and 10833003) and the National Key Basic Research Science Foundation of China (2007CB815403).

REFERENCES

Arce, H. G., Shepherd, D., Gueth, F., Lee, C.-F., Bachiller, R., Rosen, A., & Beuther, H. 2007, in Protostars and Planets V, ed. B. Reipurth, D. Jewitt, & K. Keil (Tucson, AZ: Univ. Arizona Press), 245
Bachiller, R., & Perez Gutierrez, M. 1997, ApJ, 487, L93
Churchwell, E. 1999, in NATO ASIC Proc. 540, The Origin of Stars and Planetary Systems, ed. C. J. Lada & N. D. Kylafis (Dordrecht: Kluwer), 515
Churchwell, E. 2002, ARA&A, 40, 27
Garay, G., & Lizano, S. 1999, PASP, 111, 1049
Gaume, R. A., Johnston, K. J., & Wilson, T. L. 1993, ApJ, 417, 645
Ho, P. T. P., & Young, L. M. 1996, ApJ, 472, 742
Keto, E., & Klaassen, P. 2008, ApJ, 678, L109
Mehringer, D. M. 1994, ApJS, 91, 713
Rohlfs, K., & Wilson, T. L. (ed.) 2004, Tools of Radio Astronomy (Berlin: Springer)
Sault, R. J., Teuben, P. J., & Wright, M. C. H. 1995, in ASP Conf. Ser. 77, Astronomical Data Analysis Software and Systems IV, ed. R. A. Shaw, H. E. Payne, & J. J. E. Hayes (San Francisco, CA: ASP), 433
Scott, P. F. 1978, MNRAS, 183, 435
Shi, H., Zhao, J.-H., & Han, J. L. 2010, ApJ, 710, 843
Sollins, P. K., Zhang, Q., & Ho, P. T. P. 2004, ApJ, 606, 943
Strömgren, B. 1939, ApJ, 89, 526
Tang, Y.-W., Ho, P. T. P., Koch, P. M., Girart, J. M., Lai, S.-P., & Rao, R. 2009, ApJ, 700, 251
Xu, Y., Reid, M. J., Menten, K. M., Brunthaler, A., Zheng, X. W., & Moscadelli, L. 2009, ApJ, 693, 413
Zhang, Q., Ho, P. T. P., & Ohashi, N. 1998, ApJ, 494, 636